Supplementary Information (SI) for Nanoscale.

Supplementary Information

Synergistic Carbon Black-Supported Nickel-Iron Hydroxide Nanocomposite for Selective Electrochemical Discrimination of Dihydroxybenzene Isomers

Suman Mondal,[1] Shirsendu Mitra,[2]* Felipe Fantuzzi,[3]* Kalisadhan Mukherjee[1]*

[1] Department of Chemistry, Pandit Deendayal Energy University, Gandhinagar, Gujarat-382007, India

[2] Department of Chemical Engineering, Pandit Deendayal Energy University, Gandhinagar, Gujarat-382007, India

[3] Supramolecular, Interfacial and Synthetic Chemistry, School of Natural Sciences, University of Kent, Park Wood Rd, Canterbury CT2 7NH, UK

*S.M. (Email: Shirsendu.Mitra@sot.pdpu.ac.in)

*F.F. (Email: f.fantuzzi@kent.ac.uk)

*K.M. (Email: kalisadhan.mukherjee@sot.pdpu.ac.in)

S1. Additional Experimental Details

S1.1. Materials and Reagents

Catechol (CT) and hydroquinone (HQ) were purchased from Sigma-Aldrich. Nickel(II) nitrate hexahydrate ($Ni(NO_3)_2 \cdot 6H_2O$; Sigma Aldrich, India), iron(III) nitrate nonahydrate ($Fe(NO_3)_3 \cdot 9H_2O$), triethyl amine ($N(CH_2CH_3)_3$), ethanol (CH_3CH_2OH), potassium di-hydrogen ortho-phosphate (KH_2PO_4), dipotassium hydrogen phosphate (K_2HPO_4, anhydrous), ammonium chloride (NH_4Cl), and other reagents were purchased from SRL chemicals. Electrodes (glassy carbon, platinum wire, and Ag/AgCl) were procured from Global Nanotech (India). All chemicals utilized in this study were of analytical grade and used as received. A phosphate buffer solution (PBS) served as the supporting electrolyte, and deionized (DI) water was used to prepare all aqueous solutions.

S1.2. Preparation of Phosphate Buffer Solutions (PBS)

A 0.1 M phosphate buffer at pH 7.0 was prepared by dissolving 21.75 g of K_2HPO_4, 8.50 g of KH_2PO_4, and 1.70 g of NH_4Cl in double-distilled water, followed by dilution to a final volume of 1 L. For pH adjustments, aliquots of this buffer were modified to pH 5.0, pH 6.0 or pH 8.0 using dilute H_2SO_4 or NaOH solutions. All buffers were freshly prepared or stored at 4 °C, then allowed to reach room temperature before use. The measured pH values are shown in Figure S1.

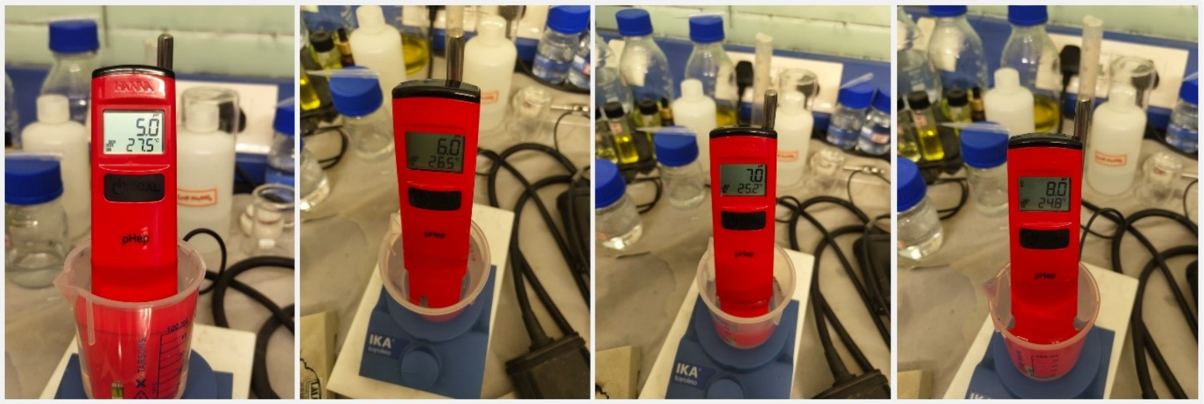

Figure S1. Measured pH values of the prepared phosphate buffer solutions (PBS) at pH 5.0, 6.0, 7.0, and 8.0, used in the electrochemical experiments.

S1.3. Instruments for Structural Characterisations and Measurement Inputs

Structural and crystallinity analyses were carried out using a Rigaku X-ray diffractometer equipped with a Cu Kα radiation source, operated at a scan rate of 3° min^{-1} over a 2θ range of 20–80°. Raman spectra were recorded using a Renishaw inVia micro-Raman spectrophotometer (UK) with a 514.4 nm excitation laser. Surface morphology and microstructural features of the nanoparticles were examined using a field-emission scanning electron microscope (Apreo 2S, Thermo Fisher Scientific, USA). Elemental composition and chemical state evaluation were obtained by XPS using a Thermo ESCALAB 250 instrument (Thermo Fisher Scientific, USA). FTIR spectra were collected using a PerkinElmer FTIR spectrometer in the wavenumber range of 400 to 4000 cm^{-1}.

S1.4. Phase evolution from hydroxide precursor to crystalline $NiFe_2O_4$ upon high-temperature calcination

the calcined samples show progressive crystallization with increasing temperature. The NF-400 PXRD pattern (**Figure S2**) reflects the onset of structural reorganization without the establishment of long-range order, while the sample calcined at 600 °C (NF-600) exhibits sharp and well-defined diffraction peaks that can be indexed to the (111), (220), (311), (400), (422), (511), and (440) planes of inverse spinel $NiFe_2O_4$ (JCPDS No. 44-1485) with Fd-3m space group . The Rietveld-refined PXRD pattern of NF-600 shows excellent agreement between the experimental and calculated profiles where the refinement was performed assuming the conventional inverse-spinel cation distribution of $NiFe_2O_4$. The outcomes is validating the structural integrity of the spinel lattice with refined lattice parameters $a = b = c = 8.3381$ Å. The marked increase in peak intensity and peak sharpening upon calcination reflects grain growth and the effective removal of residual hydroxide and organic species. Overall, these results demonstrate that the precursor NFH xerogel undergoes sequential thermal decomposition and structural reorganization, transforming from an amorphous nickel–iron mixed hydroxide matrix into crystalline $NiFe_2O_4$ structure upon calcination at 600 °C.

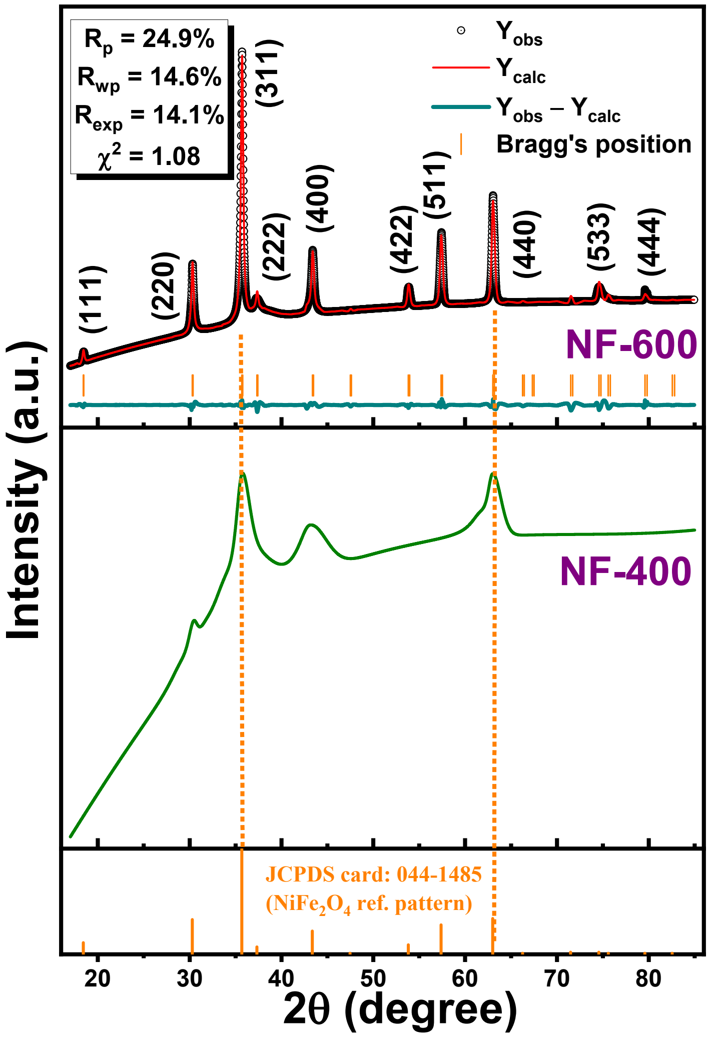

Figure S2. PXRD pattern of as-synthesized NFH hydroxide calcined at 400 °C (NF-400) and 600 °C (NF-600), illustrating the progressive phase transformation from a poorly crystalline nickel–iron mixed hydroxide matrix to a crystalline $NiFe_2O_4$ structure upon high-temperature calcination at 600 °C.

S1.5. N_2 Adsorption-Desorption Study.

The specific surface area, pore size distribution, and pore volume of the CB/NFH composites with different carbon black contents were evaluated using the BET (Brunauer-Emmett-Teller) and BJH (Barrett-Joyner-Halenda) methods based on nitrogen adsorption-desorption measurements. The N_2 adsorption-desorption isotherms shown in **Figure S3a-c** display characteristics close to Type IV isotherms with an H3 hysteresis loop, indicating the presence of predominantly microporous structures accompanied by narrow slit-like pores formed due to the aggregation of carbon black and NFH nanostructures.[1] [2]Such behaviour arises from the strong interaction between the adsorbate N_2 molecules and the carbonaceous surface of the composite materials. The H3 hysteresis loop observed at relatively higher pressures ($P/P_0 >$ 0.4) suggests the presence of narrow slit-shaped pores typically associated with carbon-based materials. The BET surface area values derived from the adsorption isotherms are summarized in **Table S1**. The 10% CB/NFH composite exhibits a specific surface area of 160.61 m^2/g, which increases significantly to 243.65 m^2/g for the 30% CB/NFH sample, indicating improved dispersion of NFH nanoparticles within the conductive carbon network. However, further increasing the carbon black content to 50% leads to a decrease in surface area to 118.02 m^2/g, which may be attributed to partial pore blocking or agglomeration effects that reduce the accessible adsorption sites.

Additionally, the pore size distribution curves calculated using the BJH method (Figure S3d-f) indicate average pore diameters in the range of ~ 3-4 nm, while the corresponding pore volumes are 0.067, 0.105, and 0.085 cm^3/g for 10%, 30%, and 50% CB/NFH composites, respectively. Among these samples, the 30% CB/NFH composite exhibits the highest surface area and pore volume, providing a larger number of accessible active sites and facilitating efficient mass transport pathways. This optimized porous structure enhances electrolyte diffusion and electron transport within the composite, which contributes to the superior performance observed for the 30% CB/NFH material.

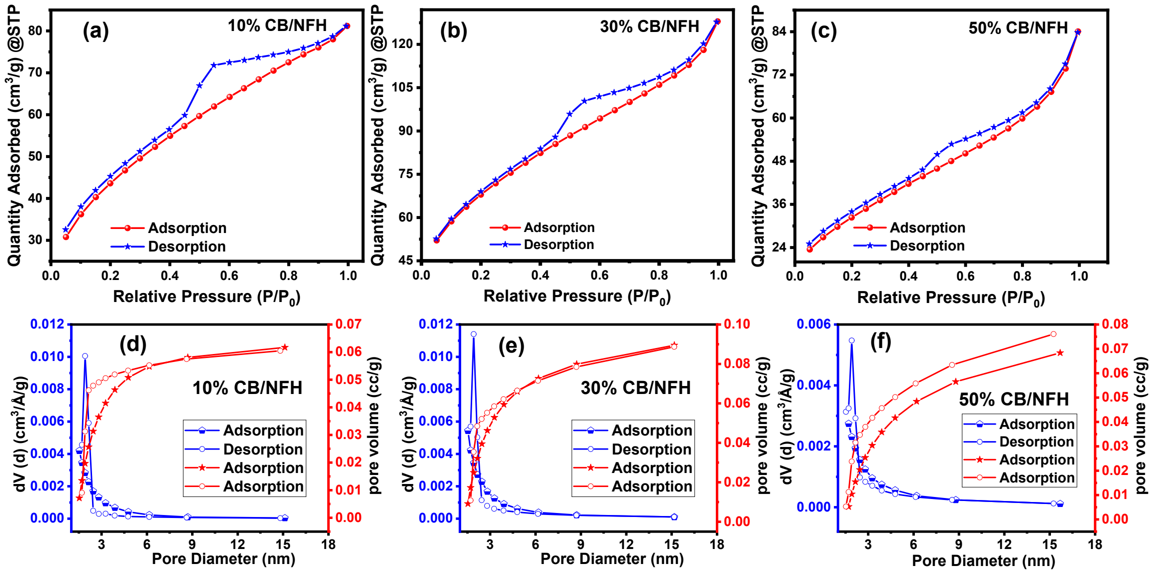

Figure S3. (a)-(c) N_2 adsorption and desorption isotherms and (d)-(f) pore size and pore volume distribution profiles of CB/NFH composites with different carbon black (CB) ratios (CB 10%, CB 30% and CB 50%)

Table S1 BET surface area and BJH pore size / pore volume values of composites CB/NFH composites with different carbon black (CB) ratios (CB 10%, CB 30% and CB 50%)

Sample Composition	**BET Surface Area (m^2/g)**	**Pore diameter (nm)**		**Pore volume (cm^3/g)**	
		BJH		BJH	
		Adsorption	Desorption	Adsorption	Desorption
10% CB/NFH	160.61	3.059	3.824	0.067	0.065
30% CB/NFH	243.65	3.061	3.818	0.105	0.101
50% CB/NFH	118.02	3.412	3.814	0.085	0.090

S1.6. Electrochemical Sensing Studies

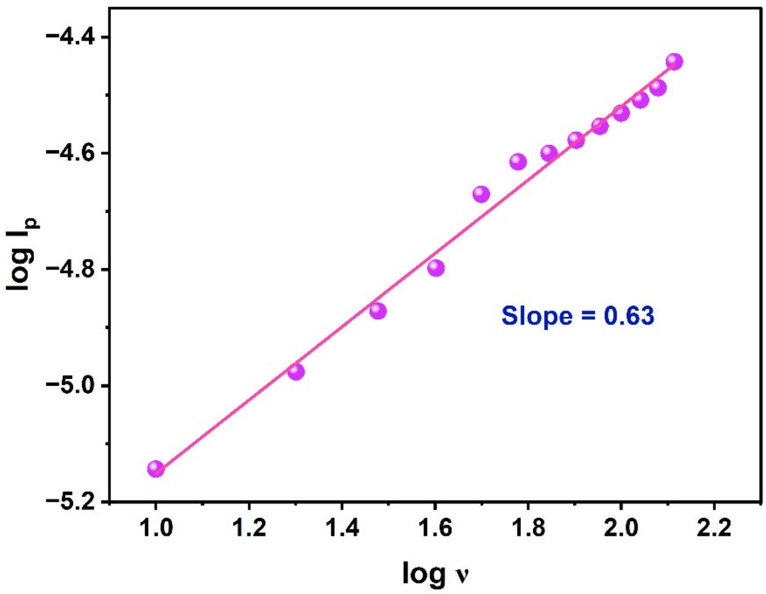

Figure S4. log–log plot of peak current versus scan rate

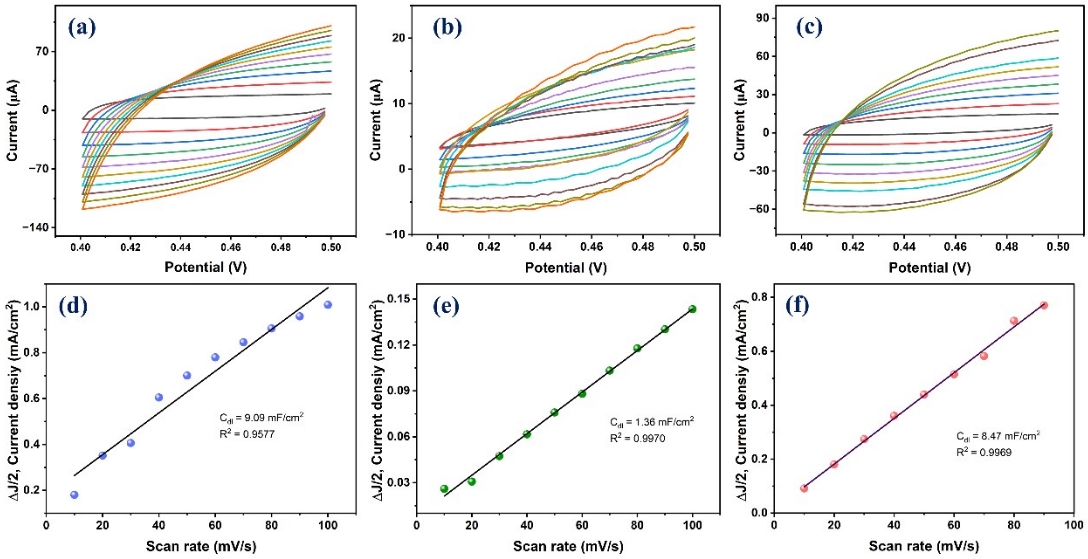

Figure S5. Scan rate-dependent cyclic voltammetry and corresponding double-layer capacitance (Cdl) analysis of (a,d) CB, (b,e) NFH, and (c,f) 30% CB–NFH composite.

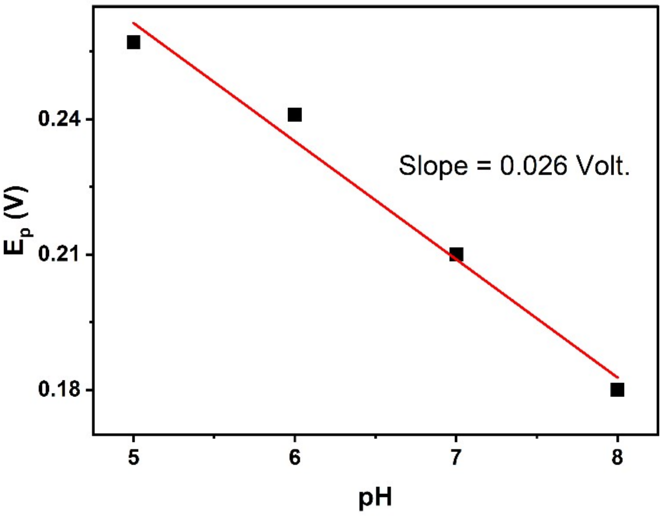

Figure S6. Ep values plotted against pH

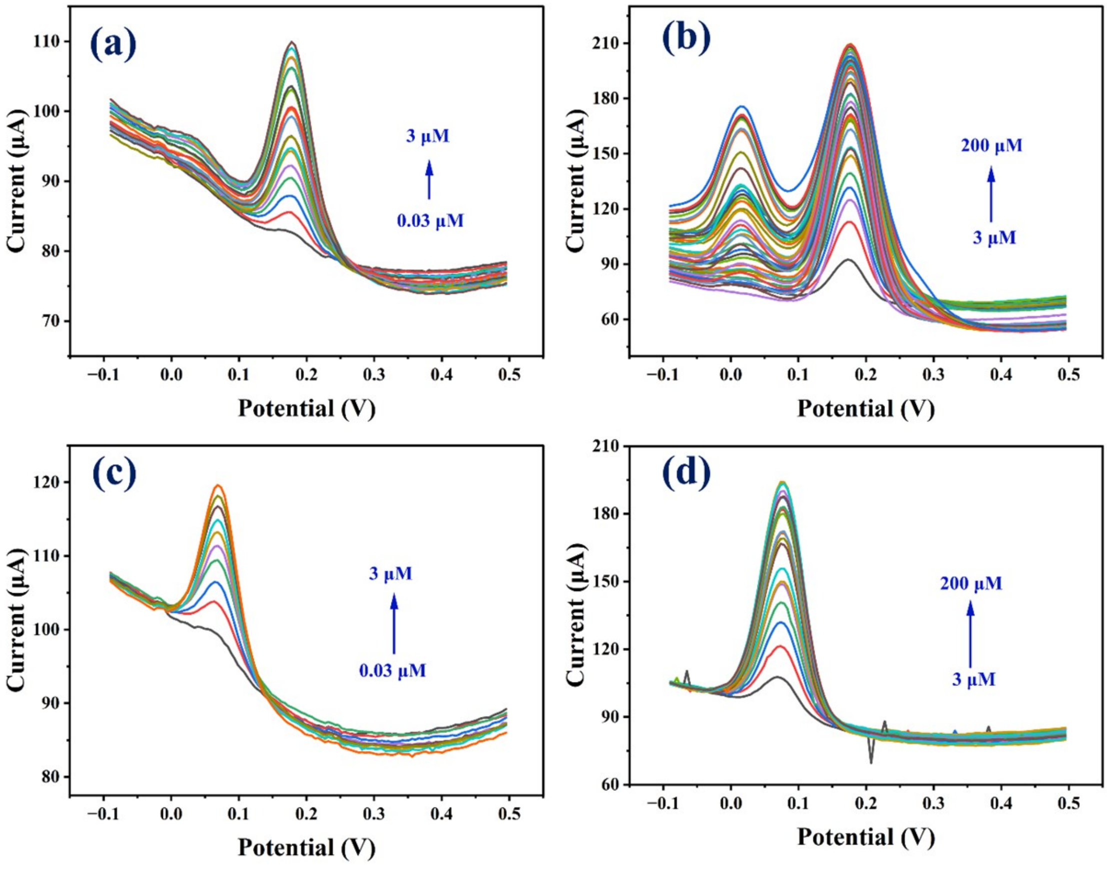

Figure S7. DPV recorded at the 30% CB/NFH-modified GCE for catechol detection in the concentration range of (a) 0.03–3 µM (b) 3–200 µM. hydroquinone detection in the concentration range of (c) 0.03–3 µM, and (d) 3–200 µM.

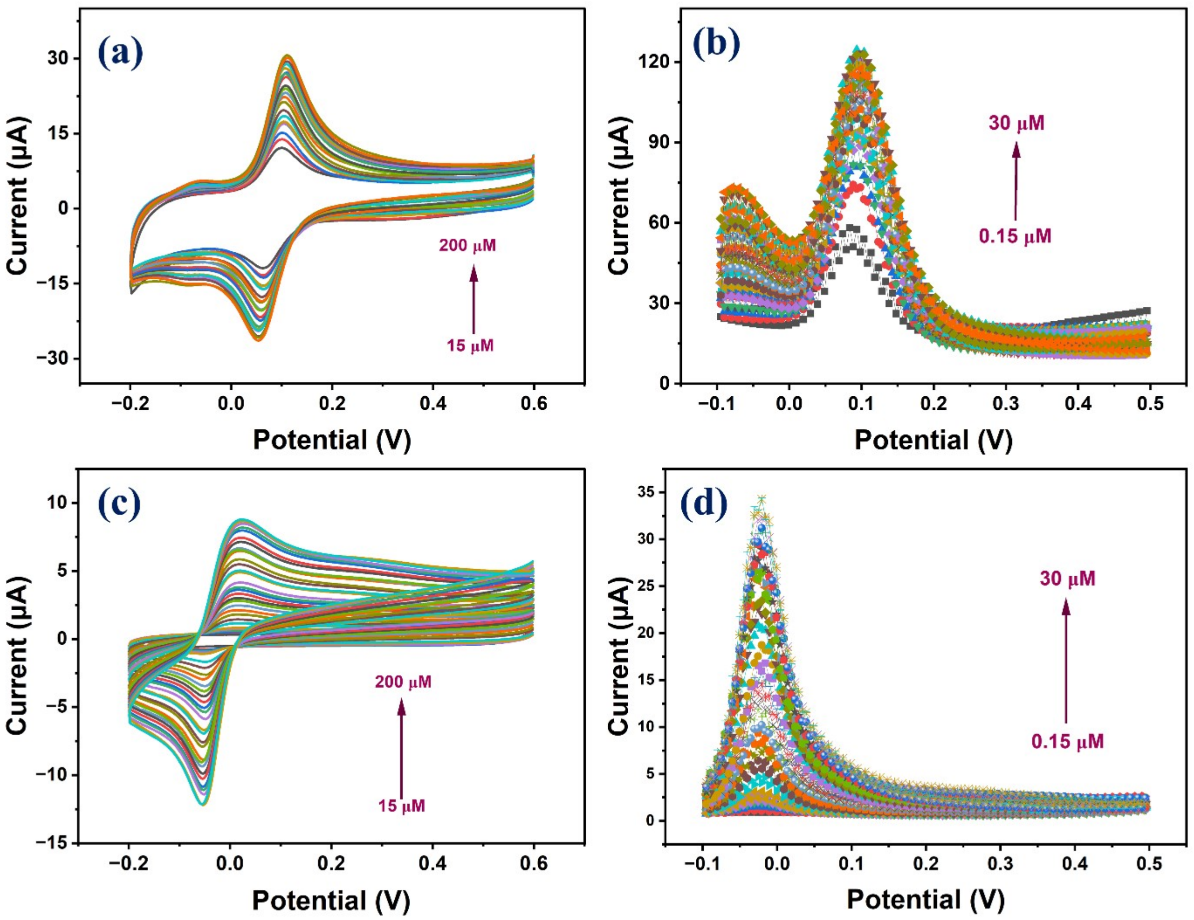

Figure S8. Electrochemical responses recorded at the 30% CB/NFH-modified SPCE for (a) CV detection of catechol in the concentration range of 15–200 μM, (b) SWV detection of catechol in the lower concentration range of 0.15–30 μM, (c) CV detection of hydroquinone in the concentration range of 15–200 μM, and (d) SWV detection of hydroquinone in the range of 0.15–30 μM.

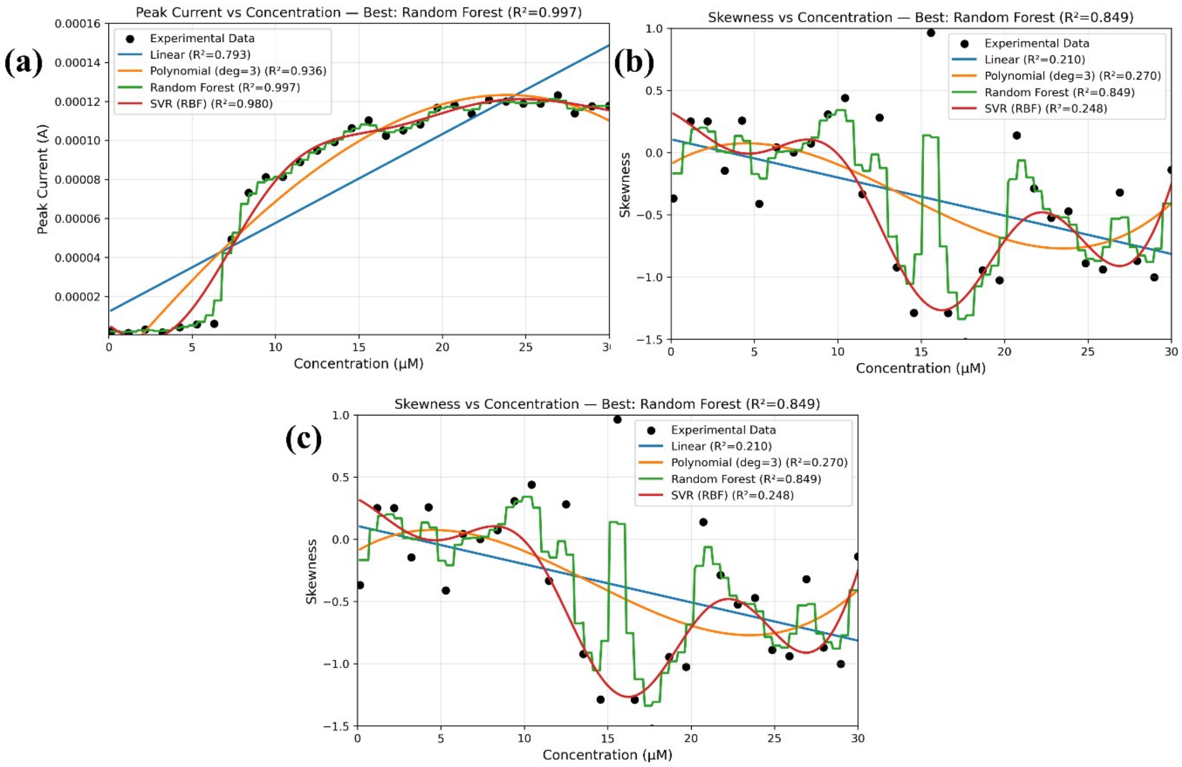

Figure S9. Scatter plots (black circles) showing the variation of (a) peak current, (b) peak skewness, and (c) peak kurtosis as a function of catechol concentration. The experimental data are fitted using different machine-learning models, including linear regression, polynomial regression, random forest, and support vector regression (SVR) with a radial basis function (RBF) kernel.

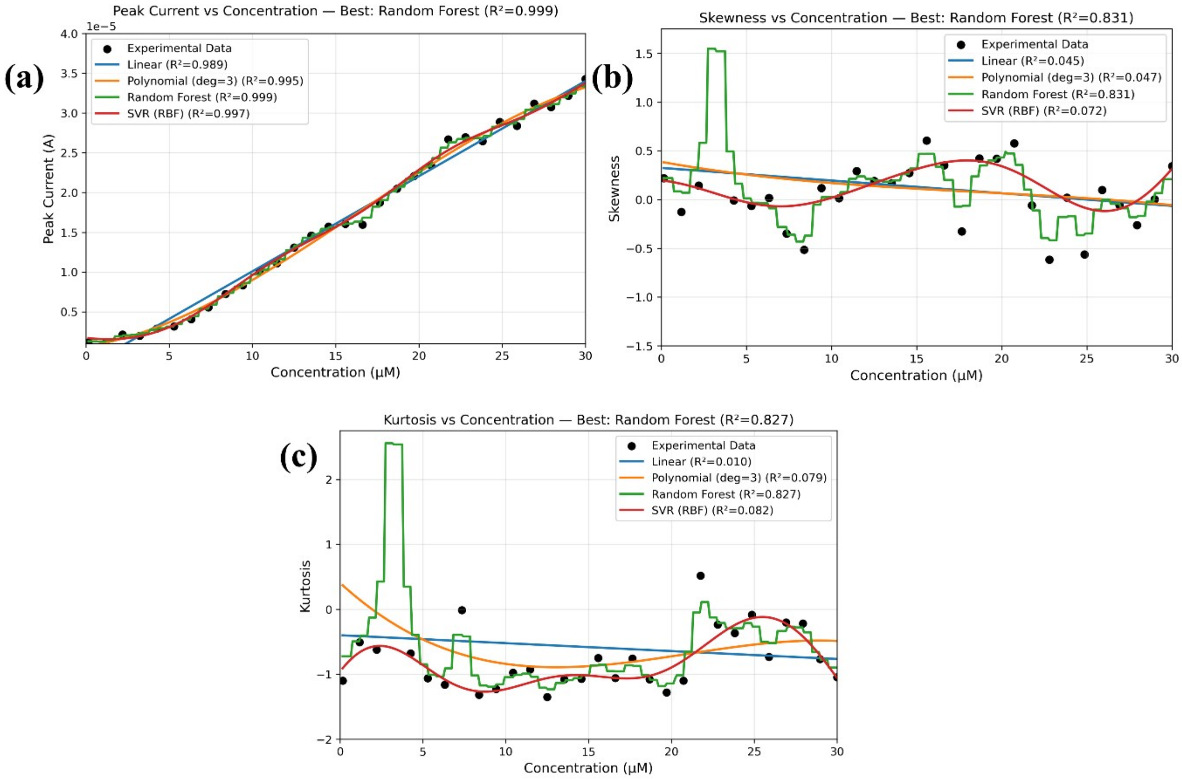

Figure S10. Scatter plots (black circles) showing the variation of (a) peak current, (b) peak skewness, and (c) peak kurtosis as a function of hydroquinone concentration. The experimental data are fitted using different machine-learning models, including linear regression, polynomial regression, random forest, and support vector regression (SVR) with a radial basis function (RBF) kernel.

Table S2. A tabular comparison of sensor material, linear range and LoD.

Sensor Material/Electrode	Linear Range (µM)	LOD (µM)	Reference
Ultrathin vanadyl phosphate ($VOPO_4$) nanosheets / GCE	0.05-120	CT- 0.0001 HQ- 0.0007	3
Cd-MOF Electrode	0.5 - 4000	0.067 HQ 0.053 CT	4
Co–Fe layered double hydroxide / GCE	0.0025 –12	0.001	5
Gold nanoparticles/chitosan @ N,S Co-doped MWCNT	0.04 -100	0.008 HQ 0.003 CT	6
ZrO210Sc/SPCE	0 -100	0.92HQ 0.69CT	7
Palladiumnanoparticles/ poly(bromocresolgreen)modifiedglassy carbonelectrode	0.2 - 200	0.08 HQ 0.07 CT	8
ITO/APTES/r-GO@Au electrode	-	1.41 HQ 1.95 HQ	9
CB-NFH/GCE	10 - 400	0.01	This Work
CB-NFH/SPCE	15 - 200	0.05	

Table S3. A tabular comparison of spike recovery of real sample

Sample	Added (µM)	Current (A)	Found (µM)	Recovery (%)
River water	10	2.48719E-5	8.09	74.9
River water	13.7	2.90083E-5	13.43	98.1
River water	16.6	3.29814E-5	18.56	111.9
River water	19.5	3.60473E-5	22.52	115.7
River water	22.4	3.90966E-5	26.46	118.3
River water	25.2	4.16388E-5	29.74	117.7
River water	28.1	4.36249E-5	32.31	114.7
River water	31.5	4.60218E-5	35.40	114.0
River water	33.9	4.78312E-5	37.74	111.2
River water	36.8	4.94190E-5	39.79	108.0
River water	39.7	5.12474E-5	42.15	106.1
River water	42.6	5.26180E-5	43.92	103.0
River water	45.5	5.48902E-5	46.86	102.9

References

1. Zhang, F.; Ma, H.; Chen, J.; Li, G.-D.; Zhang, Y.; Chen, J.-S., Preparation and gas storage of high surface area microporous carbon derived from biomass source cornstalks. *Bioresource Technology* **2008,** *99* (11), 4803-4808.
2. Ramesh, T.; Rajalakshmi, N.; Dhathathreyan, K. S., Synthesis and characterization of activated carbon from jute fibers for hydrogen storage. *Renewable Energy and Environmental Sustainability* **2017,** *2*, 4.
3. Patel, R.; Singh, V. P.; Hoque, A.; K, H.; Gaur, U. K.; Sharma, M., Ultrathin Layered Vanadyl Phosphate Nanosheets as an Ultrasensitive Electrochemical Sensor for Dihydroxybenzene Isomers in Biological and Environmental Matrices. *ACS Applied Nano Materials* **2025,** *9* (1), 178-189.
4. Huang, W.; Zhang, Z.; Li, Q.; Wang, D.; Xiong, S.; Jiang, X.; Zhou, Y.; Zhao, Q., Metal–Organic Framework-Based Dual-Mode Electrochemical Sensor for Simultaneous Electrochemical Determination of Hydroquinone and Catechol. *Inorganic Chemistry* **2025,** *64* (32), 16564-16571.
5. Mashhadizadeh, M. H.; Heydarzad, M., Development of novel electrochemical sensor based on Co-Fe layered double hydroxide for simultaneous determination of Hydroquinone, Catechol, and Resorcinol. *Microchemical Journal* **2024,** *206*, 111437.
6. Ahmed, Y. M.; Eldin, M. A.; Galal, A.; Atta, N. F., Electrochemical sensor based on PEDOT/CNTs-graphene oxide for simultaneous determination of hazardous hydroquinone, catechol, and nitrite in real water samples. *Scientific Reports* **2024,** *14* (1), 5654.
7. Ferlazzo, A.; Gulino, A.; Neri, G., Scandia-doped zirconia for the electrochemical detection of hazardous dihydroxybenzene (DHB) isomers in water. *Environmental Science: Advances* **2024,** *3* (10), 1392-1399.
8. Koçak, Ç. C., Simultaneous and sensitive determination of hydroquinone, catechol, and resorcinol with a palladium nanoparticles/poly (bromocresol green) modified glassy carbon electrode. *Analytical Methods* **2025,** *17* (27), 5662-5671.
9. Wang, G.; Zhang, S.; Wu, Q.; Zhu, J.; Chen, S.; Lei, Y.; Li, Y.; Yi, H.; Chen, L.; Shi, Z.-Q., Simultaneous detection of acetaminophen, catechol and hydroquinone using a graphene-assisted electrochemical sensor. *RSC advances* **2022,** *12* (37), 23762-23768.